Surveys in Geophysics
https://doi.org/10.1007/s10712-025-09920-9

Unconventional Three-Dimensional Active Seismic Tomography Applied in the Lousal Mine (Iberian Pyrite Belt, Portugal)

Ines Hamak[1] · Pedro Teixeira[1] · José Borges[1] · Ivan Koulakov[2,3] · Rui Oliveira[6] · Bento Caldeira[1] · Mourad Bezzeghoud[1] · João X. Matos[4] · Sofia Andringa[5]

Received: 15 April 2025 / Accepted: 8 December 2025

Abstract
The Lousal Mine (Iberian Pyrite Belt, Portugal) was operated from 1900 to 1988 for the extraction of massive sulphides and was later rehabilitated as a science museum. It was selected as a test site for underground muon tomography applied to geophysical surveys, as part of the LouMu project. This study focuses on seismic tomography to analyse the subsurface above the mine gallery, primarily surveyed by a muography telescope, which was developed specifically for this site by the Laboratory of Instrumentation and Experimental Particle Physics. To validate the muon tomography results, an initial approach using conventional 2D seismic refraction failed to reach the Waldemar gallery depth, due to limited seismic ray coverage. Therefore, an innovative setup using surface shots and in-gallery geophones was implemented, providing full ray coverage. A 3D velocity model was then produced using the ATOM3D code, which enabled the integration of this configuration and performed travel-time inversion for velocity calculation. A regional dextral strike-slip fault, the Corona Fault (CF), crosses the surveyed area, and served as the main focus of this investigation. The 3D velocity model successfully detected this structure, that corresponded to the boundary between positive anomalies of the Volcano-Sedimentary Complex (VSC) and negative anomalies of the Phyllite-Quartzite Group (PQG). The absolute velocity distribution showed a distinct offset around the Corona Fault (CF), indicating a dextral strike-slip mechanism. A subvertical extension of secondary faults was observed, reflecting deformation similar to that of the main tectonic context. Previous data from the gallery confirmed that these results are consistent with the known geology and can serve as a reference for the muon tomography interpretations.

Keywords Active seismic tomography · 3D inversion · Rayfract · ATOM3D · PROFIT · Lousal Mine · Seismic surveys

Highlights

Extended author information available on the last page of the article

- Generation of the first 3D P-velocity model of the Lousal Mine subsurface, which can now be considered as a reference model for future muographic interpretation
- How to overcome challenges in obtaining a high-resolution velocity model using a 3D innovative geometry, when 2D conventional refraction profiles are unsuccessful, in the case of accessible mines
- Detection of the vertical and horizontal spatial extension of the main Corona fault and the secondary brittle structures

1 Introduction

Conventional and unconventional active seismic tomographies were carried out in the Lousal Mine (Ermidas do Sado, Portugal) as part of the geophysical study conducted within the scope of the LouMu project (https://pages.lip.pt/loumu/en/loumu/). This project is a national collaboration between the Laboratory of Instrumentation and Experimental Particle Physics (LIP), the University of Évora, the Lousal Ciência Viva Centre, and the National Laboratory of Energy and Geology (LNEG). The project aims to develop muon tomography—or simply muography—as an accessible survey technique for geophysical applications within the national context of available geophysical tools (Teixeira et al. 2022).

To help confirm the robustness of the muon tomography results, previously generated by Teixeira et al. (2022), and produce a reference model for the interpretation, classical geophysical methodologies were employed, providing insights into the subsurface structure of the mine area. The muography survey used a muon telescope, comprising four horizontal particle detectors, that was installed inside one of the mine gallery storage rooms, in the same location as where the seismic surveys were later conducted (Fig. 1). Muography is an X-ray-like technique sensitive to rock density and capable of performing large-scale surveys.

The research area is located in the southern sector of the Lousal Mine, which includes the old Waldemar mine gallery, connecting the open pit with the South and Extreme South massive ore lenses (Matos 2021). Along this gallery, mineralisation hosts rocks are identified as belonging to the Volcano-Sedimentary Complex (VSC)—composed of felsic volcanic rocks and black shales—and the Phyllite-Quartzite Group (PQG)—characterised by quartzite deposits—both emplaced during the late Famennian period (Matos 2021). In the Lousal Mine southern sector, the Paleozoic basement is crossed by a regional geological dextral strike-slip fault (late Variscan/Eo-Alpine with an NNE–SSW orientation), named the *Corona Fault (CF)* (Relvas et al. 2012; Matos 2021). This fault exhibits normal movement, with the western block downthrown, and crosses the Waldemar gallery near the two southern concrete rooms, where it appears as a large, metre-scale subvertical fault gouge zone. The fault displacement created lithological contrasts in the area, and the site was selected to evaluate the performance of the muon telescope. The terrain above the storage room was surveyed from two different positions. The CF was observed by measuring the attenuation of muons travelling from the atmosphere, where the particles are produced, to the telescope located below the surface at the detection site (Duarte et al. 2024; Teixeira et al. 2024).

One of the classical geophysical methodologies used was the *active seismic tomography*, known as one of the most sensitive approaches for detecting geological contrasts. This technique was employed to detect the CF and to validate the reliability of the

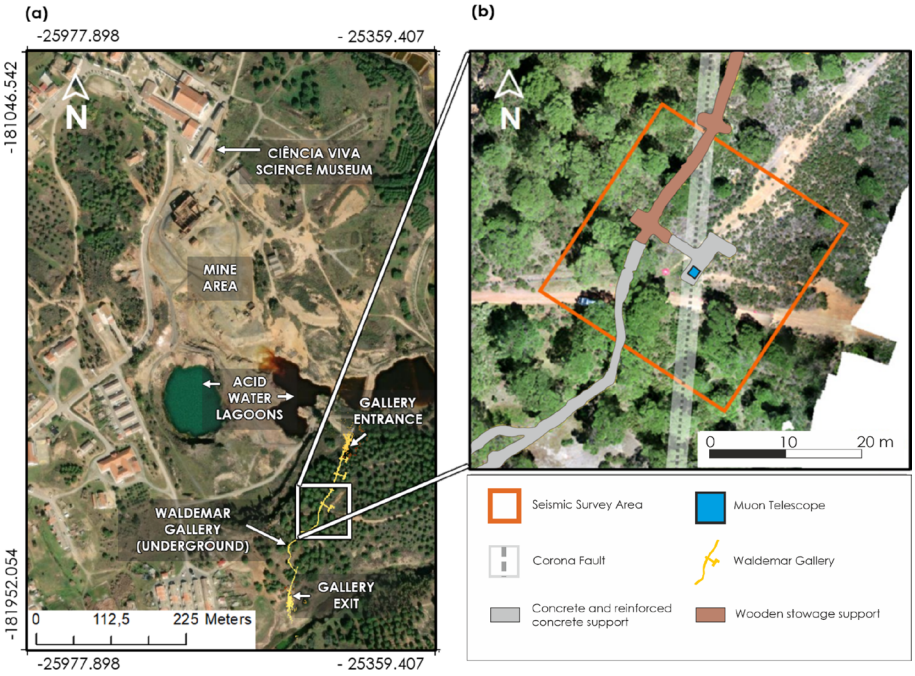

Fig. 1 **a** Location of the surveyed area in the Lousal mine, highlighted with a *white square*; **b** the area where the seismic survey was conducted with information about the type of support used to maintain the gallery tunnels and chambers stable. The coordinate system used in the maps is UTM ETRS89 (Portugal TM 06)

density model provided by the muography study. A 2D seismic refraction profile was primarily deployed across the CF in the area. It had the purpose of obtaining an image of the subsurface, between the surface level and the Waldemar gallery depth, located at approximately 18 m depth. The data analysis revealed that the seismic rays did not reach the mine gallery, probably due to slight variations in seismic velocity in deep layers, which prevented effective refraction of the waves emitted by the seismic source (a 6 kg hammer). Therefore, an innovative 3D source–receiver configuration was chosen to ensure successful coverage of ray paths down to the depth of the gallery, as described in this paper.

The 3D seismic inversion was performed using the ATOM3D software (Active Tomography in 3D; Koulakov 2009b) to obtain the P-wave velocity distribution in three dimensions, allowing the characterisation of the subsurface structure. In addition, we aimed to evaluate the vertical extension of the fault system that outcrops at the surface and continues into the interior of the gallery, as well as to identify other subsidiary faults. As old excavations could have created fractures and weakened the geological formations surrounding the gallery, stress redistribution might have occurred, making its evaluation important (Cai et al. 2014; Friedel et al. 1995; Wang et al. 2008, 2018). Thus, as seismic tomography can help to understand the stress changes, analysing the velocity distribution within the surveyed area of the mine gallery will help to identify weaker zones that may be more prone to collapse, thereby providing additional insights into the safety of the mine.

2 Geological Settings

The Lousal Mine is located in the southwest of Portugal (northwest part of the Iberian Pyrite Belt, oriented N50ºW) within the VSC/PQG Lousal-Caveira structure (Matos et al. 2020). Its exploitation began in 1900 and ended in 1988, operating during that period for the extraction of massive sulphides, mainly pyrite ore, to depths of up to 500 m (Matos and Oliveira 2003). The mine and its surrounding area were rehabilitated by the EDM—*Empresa de Desenvolvimento Mineiro, S.A.* company, and integrated into the network of Ciência Viva public science centres, constituting a successful rehabilitation example of a closed mine (Oliveira et al. 2013; Relvas et al. 2012). The mining complex is characterised by its altered rocks, acid–water lagoons, and mine shafts (Fig. 1a). The area where the seismic surveys were carried out is located in a small sector of Lousal Mine that is crossed by the regional CF, which has been identified along a 40 km-long zone trending NNE–SSW (Matos and Relvas 2006; Oliveira et al. 2013; Matos 2021). This fault separates the VSC (western, downthrown block) from the PQG (eastern, uplifted block) and is characterised by a dextral horizontal movement that is significant but has not yet been measured (Fig. 2).

The VSC comprises different depositional sequences with thick rhyolitic–rhyodacite lavas (> 300 m), mafic volcanic rocks, and black and grey mudstone, grading upward into rhyolitic sills and ore bodies forming the ore horizon of the Lousal–Caveira Formation (Strunian, Late Famennian age). The upper VSC sequence consists of shales with nodules, siliceous shales, cherts, and mafic volcanic rocks (both intrusive and extrusive, including lavas), and purple shales. The structure forms a narrow antiform with two main ore lenses. The PQG is represented in the inner part of the antiform and consists of phyllites and quartzites belonging to the Upper Corona Unit (Late Famennian age) and Lower Corona Unit (Givetian age) (Matos 2021). The Lousal massive sulphide deposits and associated stockworksare composed of ore lenses distributed linearly over a length of 1.5 km and were the main aim of the exploitation done in the mine. The ore was composed of approximately 45.0% sulphur, 1.4% zinc, 0.8% lead, and 0.7% copper, and was known for its significant gold content (Strauss 1970; Fernandes 2011; Matos and Relvas 2006).

The Waldemar Gallery is the uppermost underground gallery of the mine complex and the only one still accessible. The gallery was excavated horizontally at a constant elevation of 52 m above sea level, allowing the connection between the mine's open pit, the South and Extreme South ore lenses, and the southern gossan zone (Matos and Oliveira 2023; Relvas et al. 2012; Matos 2021). It cuts the VSC host rocks, namely dark grey and black shales with sulphide veins (e.g. near the Waldemar shaft), and the PQG phyllites and quartzites that outcrop in the northern sector of the gallery. The tunnel, oriented NNE–SSW, extends horizontally for approximately 270 m. Considering the near-surface location of the gallery, the primary sulphide mineralisation appears completely affected by oxidation related to weathering.

To reach the base of the surveyed area inside the gallery, one must walk the first 90 m of the tunnel to reach the fourth explosives storeroom (Storage Room 4), the last one from the entrance. As mentioned before, the CF gouge zone defines the boundary between the PQG (eastern block) and the VSC (western block). Along the fault zone, intense fracturing and clays are observed. The VSC rocks show more visible decompression fractures and appear more prone to collapse compared with the section excavated in the PQG, which is sturdier and displays more intense subvertical S1 cleavage planes (Matos 2021). The different fractured zones are reflected in the way the gallery support system has been applied. The gallery walls and ceiling of the PQG section were supported mainly by wooden stowage

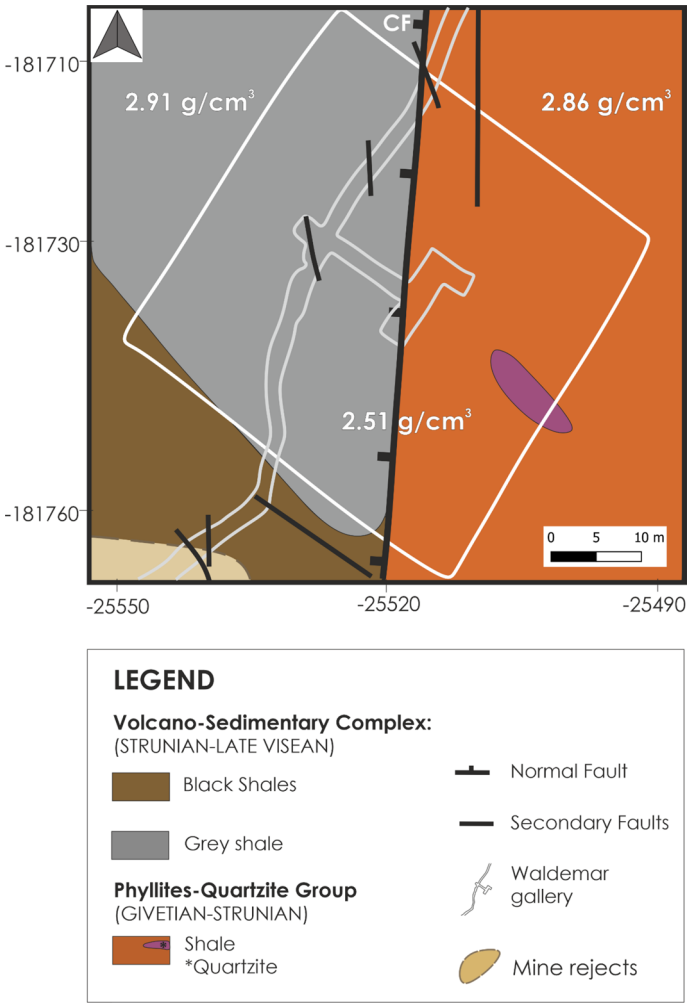

Fig. 2 Geological map adapted from Matos et al., 2022*, showing geological sequence and fault system present in the area where the 3D seismic survey was conducted, highlighted in a *white square*. (CF: Corona fault). The average density of the different geological formations is also mentioned. *Reference: Matos, J. X., et al. (2022). Lousal mine southern sector geological map, 267 1/5.000 scale. Nacional Laboratory of Energy and Geology (LNEG), LouMu Project

(e.g. near the CF), with reinforced concrete used only to cover the storage rooms (Fig. 1b). Conversely, in the VSC gallery section, concrete was used to cover the more unstable parts (e.g. secondary fault zones), with reinforced concrete in some areas (Matos and Oliveira 2003).

The CF is a subvertical late Variscan geological fault, oriented N5ºE, exhibiting a dextral strike-slip movement with a normal component (western block downthrown). It has a width of about 5 m and a surface extension of roughly 40 km, crossing an estimated depth of more than 4 km. Its tectonic movement created a system of secondary

faults in its surroundings, which are observed at the level of the gallery, following similar kinematics and defined by intense fault gouge (Matos 2021).

The underground surveyed area is highly heterogeneous, as observed in the Waldemar mine gallery. As part of the geophysical study, rock samples were collected at various locations within the gallery to obtain direct measurements of in situ rock density. The reference values were derived from the mean densities of rock samples measured using the water volume displacement method. The VSC is characterised by grey shale with a mean density of 2.91 g/cm^3, slightly higher than that of the PQG, which has a mean density of 2.86 g/cm^3. The CF zone marks the division between them and is characterised by a mean density of about 2.52 g/cm^3. Furthermore, the first 3 to 4 m of the subsurface appear more weathered and are generally characterised by a lower mean density of around 2.51 g/cm^3 (Fig. 2).

Fieldwork was carried out at the surface within a square area of 45 m × 45 m, partially covered with low vegetation, a dirt road, and several pine trees. The topography of the surveyed area varies between 66 and 72 m. Taking the altitude at the centre of the square area (71 m) as a reference, most elevation changes are within 2 m below or 1 m above that point. Only some peripheral areas show vertical variations reaching up to 5 m below the reference point (Fig. 3). The south-western part, which leads to the Waldemar mine shaft entrance below the dirt road, is an example of a section with an elevation decrease and is characterised by the accumulation of mine tailings and highly fractured material (Fig. 2).

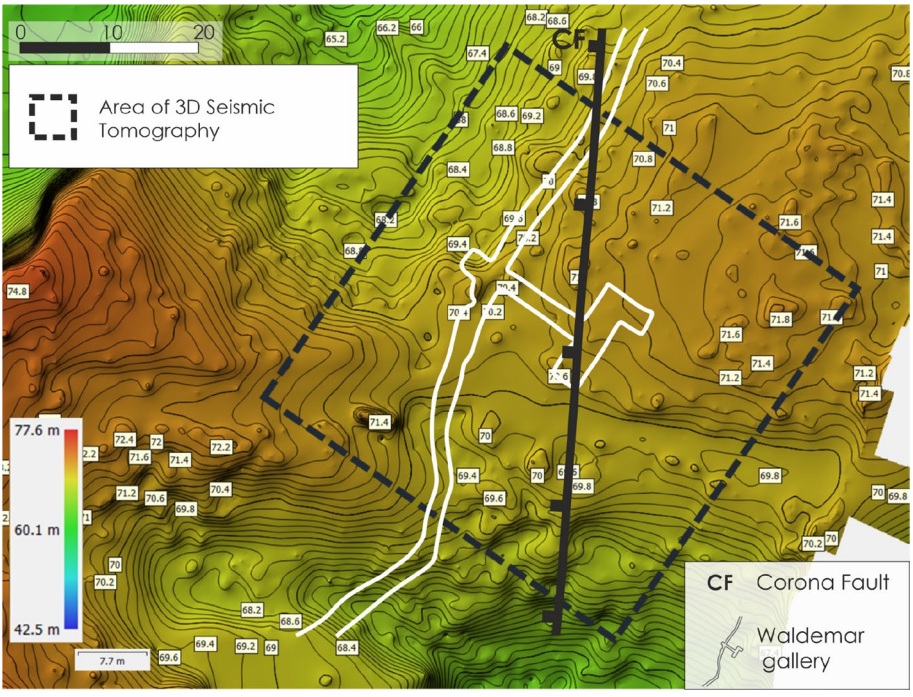

Fig. 3 Digital elevation model (DEM) map showing the variation of topography within the studied region highlighted in a *dashed square*. The *black line* represents the main Corona fault (CF), and the *white line* refers to the Waldemar gallery location

3 Data Acquisition and Analysis

Seismic refraction tomography is a widely used survey technique that performs very well in areas with significant topographic variation. It employs geophones —devices sensitive to the propagation of P-waves through the ground—which record the waves arrival times. The underground configuration of the rock layers and the geological structures cause wave reflections and refractions at contrasting interfaces. These interactions are captured by the geophones, which are connected to a recording station that logs the data for later analysis (Rucker 2000).

The two seismic surveys described in this paper used a PASI Anteo multichannel seismograph equipped with 48 vertical geophones operating at a natural frequency of 40 Hz. The first seismic campaign was conducted in May 2022 and involved acquiring a 2D seismic profile using the traditional linear configuration; however, this survey did not reach the gallery level. A second campaign was carried out in February 2023 using an innovative 3D seismic tomography approach. The main goal was to improve the understanding of the geological fault system inside the area by enhancing seismic ray coverage—a factor that is crucial for higher resolution imaging. A detailed description of both campaigns is presented below.

3.1 Conventional 2D Seismic Refraction Configuration

In the traditional setup, a 2D seismic profile, 47 m in length and oriented WNW–ESE, was acquired in the field, crossing the study area and intersecting the CF.

For this profile, the linear seismic refraction survey was carried out with a spread of 48 geophones (40 Hz) spaced 1 m apart (Fig. 4). The seismic signals were generated using a 6 kg sledgehammer striking a metal plate on the ground, at intervals of 3 m between shot points. For each shot position, the hammer strike was repeated three times to reduce noise and increase the signal-to-noise ratio. This procedure ensured that when the three recorded strikes were stacked, the coherent signal was enhanced while random noise was reduced. Consequently, the three signals were stacked to form a single seismogram used directly for first-arrival picking. However, the individual files were still analysed if corrections were needed in cases of unclear arrival times. During the ground strikes, a geophone connected independently to the seismograph terminal was placed near the metal plate and served as a trigger to initiate signal recording, known as the *trigger*.

A total of 17 shot points were acquired along the geophones' line, together with two far-offsets shots positioned 23 m from the starting and ending points of the geophones' line. After that, the field data were brought to the laboratory for waveform analysis and first-arrival picking using the seismic refraction tomography software Rayfract (Intelligent Resources Inc., 2020 version 3.36). This code was used exclusively for data processing. The distribution of seismic ray paths was provided by the software PROFIT (PROfile Forward and Inverse Tomographic modelling), created by Koulakov (2009b) and Koulakov et al. (2010). It showed a vertical resolution of 15 m, thus being unable to provide a model that could reach the targeted depth (~ 18 m), and with poor coverage of the subsurface area intended to be illuminated (Fig. 5). Therefore, an unconventional configuration of shots and geophones was chosen to generate a three-dimensional velocity distribution.

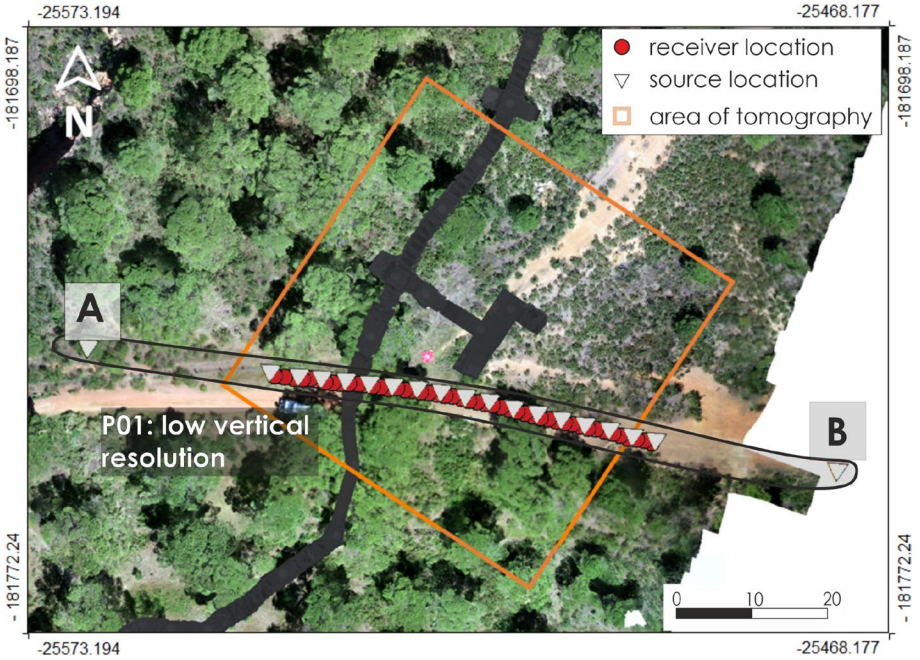

Fig. 4 Location of the two-dimensional profile where the first seismic refraction survey was conducted. *White triangles* represent the shots and *red dots*, the geophones. The *orange square* refers to the 3D seismic survey area. The *red area* highlights the location of the survey profile

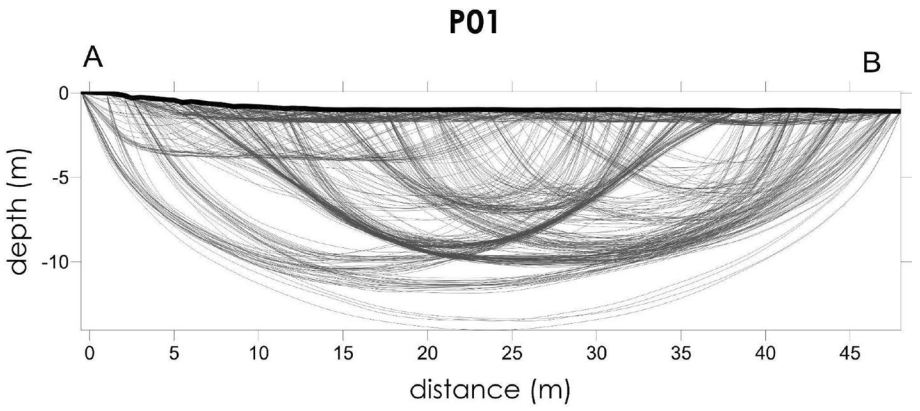

Fig. 5 Ray distribution of the first 2D profile, carried out in Lousal mine reaching a depth of approximately 15 m. This image was generated after the use of PROFIT whose detailed functioning is described in Koulakov 2009a, b, c

3.2 Development of an Unconventional Geophysical Configuration for the Enhancement of the Seismic Ray Coverage

As previously described, the 2D seismic refraction survey provided a model with incomplete coverage of the targeted terrain. Therefore, to achieve the main objective of this study, a new configuration was designed to reach greater depths and more accurately constrain the geological structures within the area.

A non-standard configuration of sources and geophones was implemented to ensure that seismic rays covered the entire subsurface. A set of 48 geophones (operating with a frequency of 40 Hz) were installed inside the gallery at 1 m intervals, and 256 artificial vibration sources (arranged in a 16×16 grid) were generated at the surface, spaced 3 m apart, forming a uniform grid of shot points covering an area of approximately 45 m×45 m (Fig. 6). A 6 kg sledgehammer striking a metal ground plate was used to produce the seismic wave propagation. The first compressional waves (P-waves) were emitted, travelling from the surface to the mine gallery depth (~18 m).

The trigger cable was extended from the gallery through the Waldemar shaft to the surface, where the shots were performed. As in the conventional seismic campaign, three hammer strikes were executed at each point to reduce the effect of the noise on the arrival time readings and thereby increase the signal-to-noise ratio. The pre-trigger was set to 10 ms, and data acquisition was carried out with a sampling frequency of 32,258 Hz and a sampling window of 100 ms.

Data processing began with the precise identification of first-arrival times using Rayfract software, followed by travel-time inversion using the ATOM3D code (Koulakov 2009a). As the signal-to-noise ratio (SNR) in the stacked files was relatively low, a band pass filter was applied to all seismograms to improve clarity. The selected filter ranged from 80 to 300 Hz (Fig. 7).

Following the detection of first-wave arrivals, quality control was conducted by assessing the picking accuracy and filtering the database to retain only coherent signals

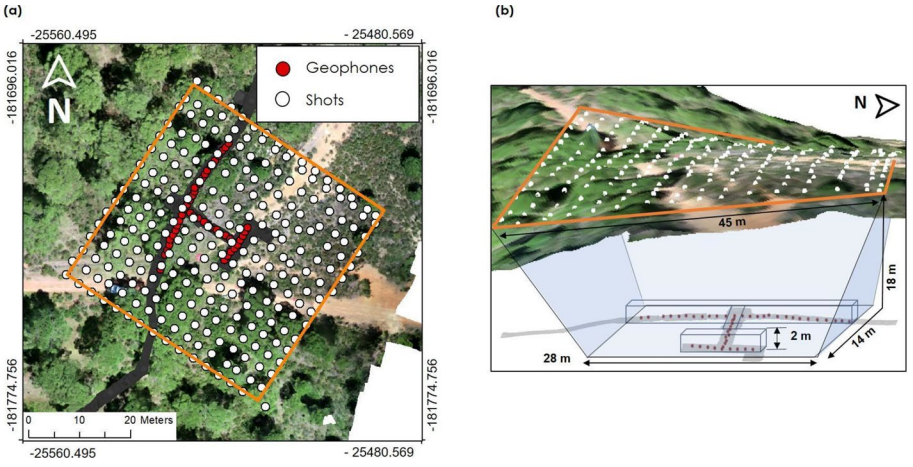

Fig. 6 **a** Representation of the unconventional configuration of shots and geophones for a three-dimensional seismic refraction survey employed in the area of interest highlighted by an *orange square*. *White dots* represent the shots executed at the surface and *red dots* the geophones installed inside the gallery; **b** the geophone-shots arrangement with the surface topography

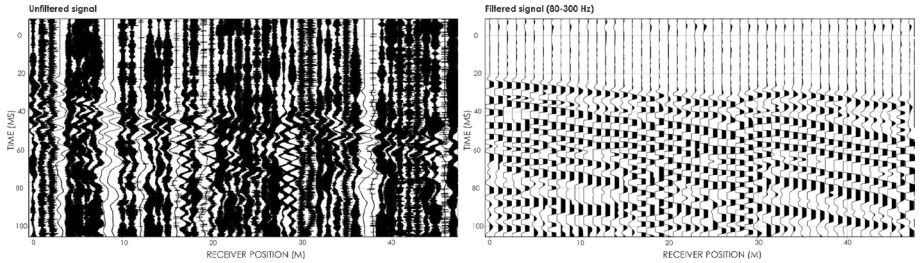

Fig. 7 Example of a raw signal and a filtered one (80–300 Hz)

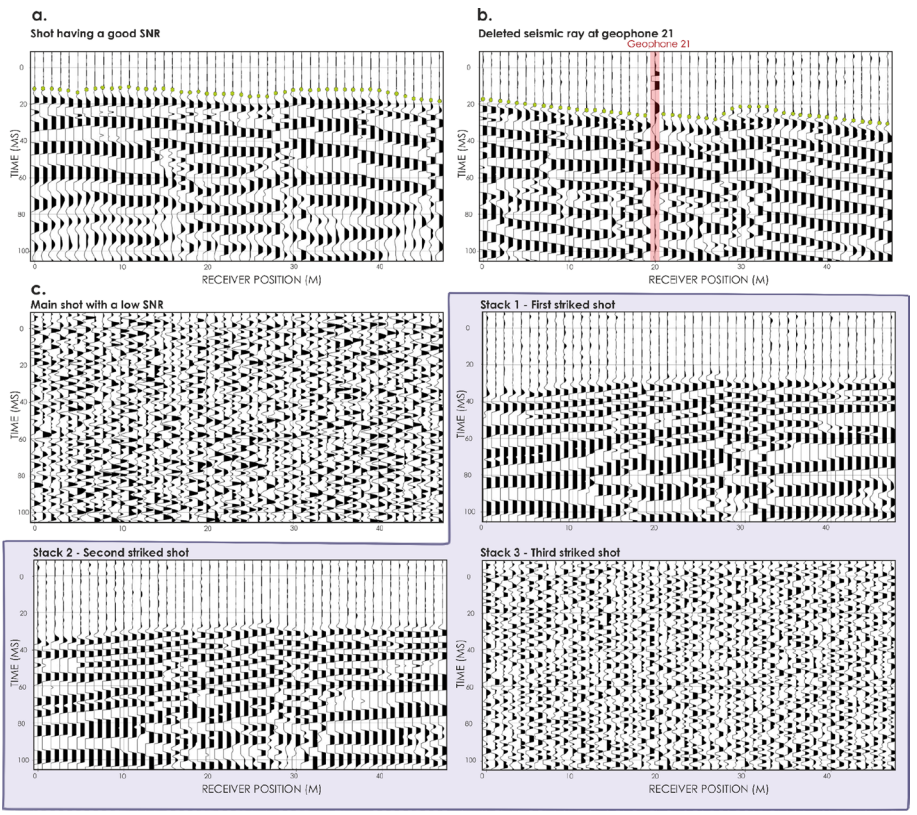

Fig. 8 **a** An example of a signal having a robust signal-to-noise ratio with an easy first-arrival reading; **b** example of a seismogram having an unclear arrival at geophone 21 and consequently removed from the database; **c** example of a noisy signal describing 2 clear (stack 1,2) and noisy stacks (stack 3). This is illustrated to give an example of how some signals were corrected by observation of individual traces. All the signals were filtered by 80–300 Hz

(Fig. 8a). After quality control, several issues were identified: some waveforms exhibited a very low signal-to-noise ratio, making the detection of first arrivals impossible (Fig. 8b). Consequently, unclear or noisy traces were removed to reduce uncertainty

in the seismic inversion. In certain cases, noisy signals (as shown in Fig. 8c) were corrected by examining the three individual traces; in such instances, it was determined that the Stack 3 (the third hammer strike) has distorted the signal. This data suppression did not compromise the density of seismic ray coverage.

4 Methodology

The 3D travel-time inversion in this study was carried out using the ATOM3D programme (Active Tomography in 3D), generating the first images of the P-wave velocity distribution inside the area of investigation. The algorithm is based on the same computational methodology and represents an adaptation of the LOTOS-09 programme (Local Tomography Software) used in passive tomography, whose detailed functioning is described in Koulakov (2009a, b, c).

This software was chosen to perform the analysis of the active seismic tomography in the Lousal Mine, owing to its ability to integrate the innovative 3D geophone-source configuration. It is user-friendly and requires relatively low computational time compared with similar software packages. The inversion process is based on an iterative approach which refines the 3D velocity model step by step, employing several algorithms dedicated to each stage of the inversion. Some of these programmes are executed throughout the entire process, while others run only during the first iteration.

The programme incorporates a ray-tracing method based on Fermat's principle, following the initial formulation proposed by Um and Thurber (1987). This method begins by tracing a rectilinear segment connecting the source to the station and progressively bending it at its midpoint to follow the path of minimum travel time (Koulakov 2009a; García-Yeguas et al. 2012). Once the ray tracing is completed, the ray density is computed and the grid parameters are defined.

The derivative matrix is then generated, and the travel-time inversion is performed using the least square method (LSQR) (Nolet 1987; Paige and Saunders 1982), yielding the three-dimensional P-wave velocity distribution. The matrix inversion minimises the difference between observed and calculated travel times, expressed as the root-mean-square error in the L1 norm (RMS).

The velocity model is computed within a grid of nodes initially spaced at regular intervals, using linear interpolation (set to 1.5 m in this case). The node spacing between nodes is adjusted during inversion according to the ray density and cannot be smaller than a predefined minimum value (set to 0.5 m). Areas with a high concentration of rays are sampled with fine node spacing, while coarse spacing is assigned to zones of lower ray density (Fig. 9a). In that case, model resolution does not depend on node spacing, but primarily on the smoothing and amplitude damping parameters, which were selected after synthetic inversion testing (see section 5.1).

To minimise the influence of grid orientation on the tomographic results, several grids with different base angles (0°, 22°, 45°, and 67°) were computed, and the results were stacked. The travel-time inversion generated velocity values that were linearly interpolated between nodes.

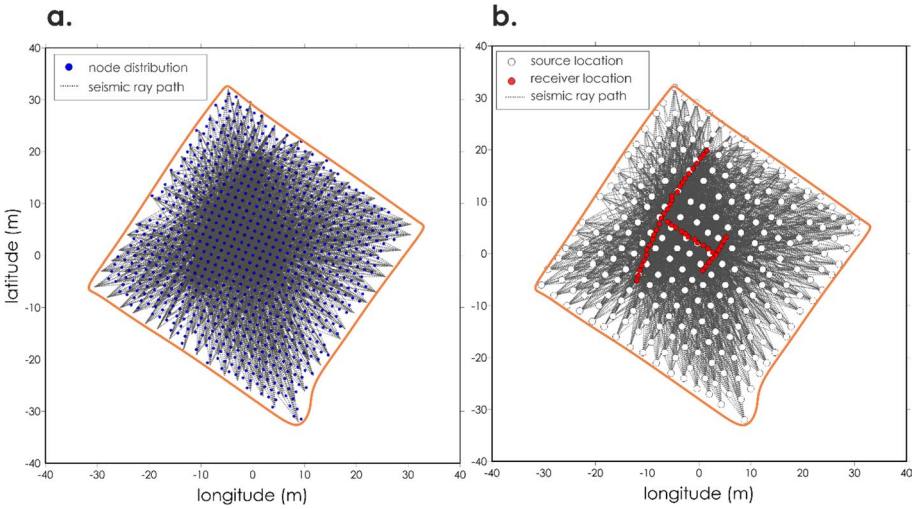

Fig. 9 3D seismic ray path distribution. **a** Node distribution and **b** geophones and shot locations. The *orange square* represents the area resolved by ray path spread

5 Results and Discussion

5.1 Synthetic Resolution Tests' Inversion

Before running the inversion with the experimental data, an assessment of the model resolution was carried out. Checkerboard sensitivity tests were performed to evaluate the inversion ability to recover specific structural details of the subsurface. The principle of this approach was to use the same source–receiver pairs and the reference 1D velocity model employed in the observational data inversion to compute synthetic travel times and analyse the recovery of imposed anomalies, thereby assessing the spatial resolution capability of the area.

Given that the artificial sources were spaced 3 m apart, robust ray coverage and strong recovery of small anomalies were expected (Fig. 9). To determine the optimal values of inversion parameters—namely amplitude damping and smoothing—which are crucial for stabilising the solution, several tests were conducted. The best reconstruction of patterns was achieved for anomalies of approximately 3 m × 3 m, using a smoothing factor of approximately 15 and an amplitude damping of 6, following the approach described in García-Yeguas et al. (2012) and Koulakov (2020). Figure 10 illustrates the reconstruction of synthetic anomalies of roughly 3 m × 3 m, 5 m × 5 m, and 7 m × 7 m, each separated by 3 m.

The synthetic tests revealed a strong reconstruction of anomalies across nearly the entire sampled volume. The unconventional positioning of geophones and sources provided a denser distribution of seismic rays above the gallery level, ensuring effective coverage of the whole subsurface with anomaly patterns. This is illustrated in Fig. 9, which shows a regular node distribution, indicating a homogenous spread of ray path, contributing to a robust coverage of the investigated area. In Fig. 10, the anomaly patterns are accurately recovered at most depth slices, except for the section format around 10 m depth, where poorer reconstruction is noted, although it improves for anomalies greater than or equal to

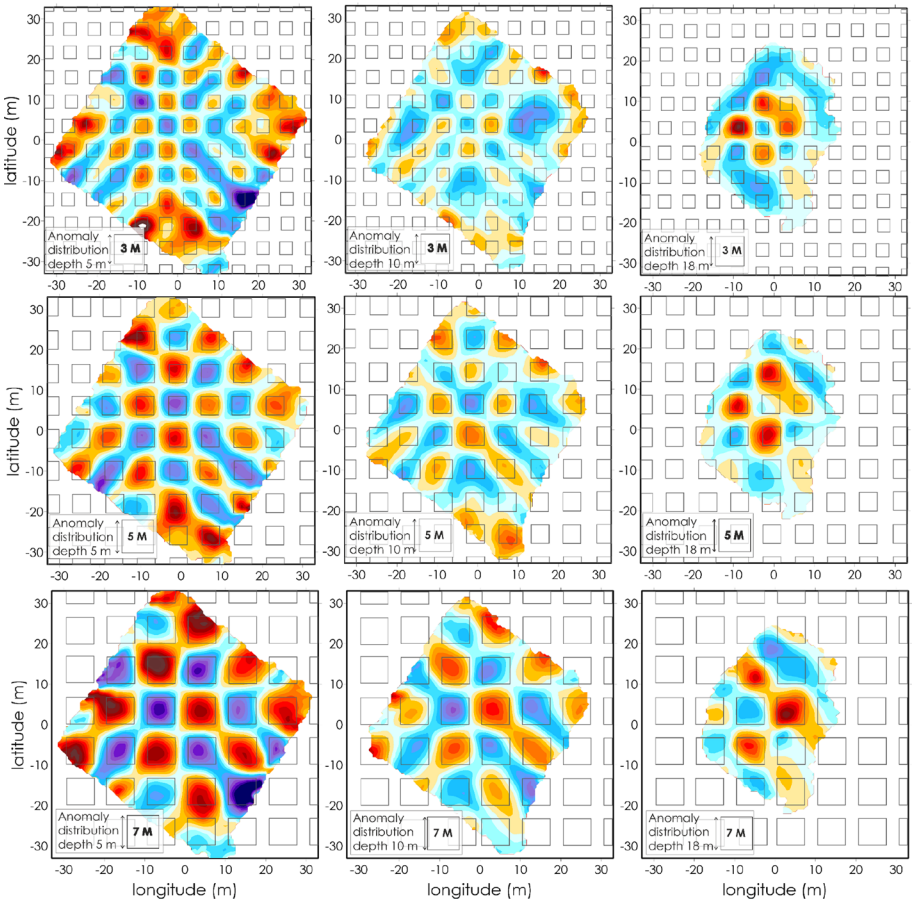

Fig. 10 Checkerboard test results for three different anomaly sizes (3 m×3 m, 5 m×5 m, and 7 m×7 m). The anomaly patterns are shown for depth slices at 5 m, 10 m, and 18 m. The squares represent the recovered anomalies' dimensions and are located on the top left side of the 5 m section

5 m×5 m. A smearing effect appears at the model edges due to a reduction in ray density with depth, resulting from the H-shaped geophone configuration imposed by the geometry of the gallery tunnels and chambers. This effect is highlighted in Fig. 9, where a pronounced concentration of ray paths occurs in the central part of the region.

An additional synthetic test was performed to assess the resolution above and below the Waldemar gallery (Fig. 11). This test involved introducing realistic anomalies derived from the experimental inversion (Fig. 11a), consisting of ± 20% alternating velocity perturbation at two depth intervals: from 2 m above sea level to 10 m and from 11 to 25 m. Following the synthetic inversion, the recovered velocity anomalies were analysed in detail (Fig. 11b).

For the upper interval (2 m above sea level to 10 m), the velocity patterns were robustly recovered across almost the entire region, showing strong correlation with the experimental inversion results (later presented in section 5.2). The negative synthetic anomalies NS1 and NS2 slightly exceeded -20% (approximately -25% to -30%), whereas

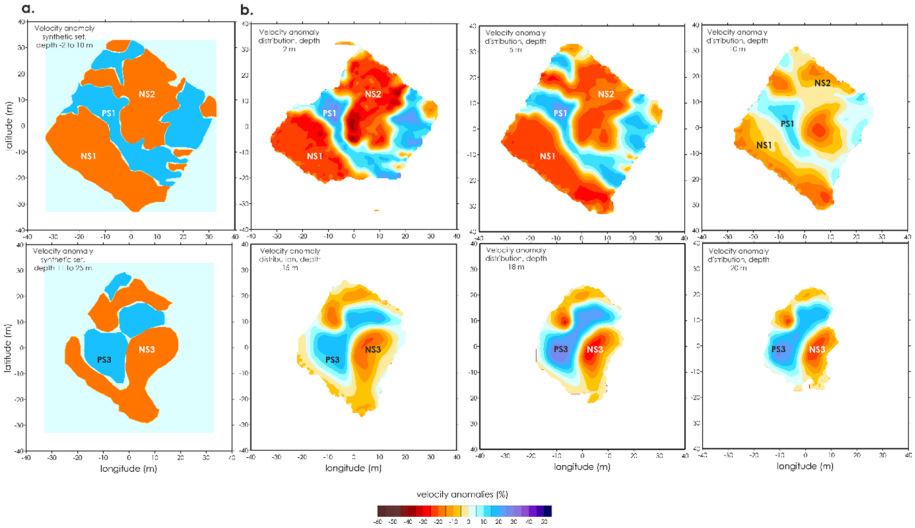

Fig. 11 Synthetic tests with free-shape realistic anomalies based on experimental inversion results. **a** Free shaped realistic anomalies designed from two different depth intervals: from 2 m above sea level to 10 m and 11 to 25 m. **b** Depth slices of velocity anomaly distribution for six different depths: 2 m, 5 m, 10 m, 15 m, 18 m, and 20 m. NS: negative synthetic anomaly, and PS: positive synthetic anomaly

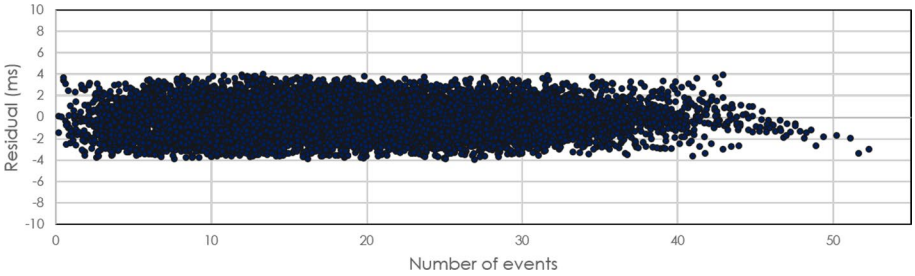

Fig. 12 RMS (root-mean-square) distribution vs. the number of events computed after the generation of the 3D velocity model at the last iteration (iteration 5) of experimental inversion

the positive synthetic patterns PS1 reached about + 20%. In the deeper interval (11 m to 25 m), the velocity anomalies were robustly reconstructed in both amplitude and shape, except for the NS3 at 18 m depth, which reached around -30% (Fig. 11). The alternation of anomaly polarity with depth was successfully retrieved, confirming robust vertical resolution. Moreover, comparison between the experimental inversion results (see section 5.2) and the free-shaped synthetic reconstructions shows a strong correspondence in anomaly patterns.

For both depth ranges, however, a peripheral smearing effect was observed, attributed to the reduced ray coverage in those areas (Fig. 9). This confirms the effectiveness of the unconventional 3D inversion configuration, which provided enhanced image resolution for nearly the entire surveyed volume, except at around 10 m depth where ray density decreases. Consequently, regions of poor resolution were carefully considered during the interpretation of experimental results to ensure reliability.

Table 1 Evolution of the RMS (root-mean-square) and the reduction variance (percentage of the residuals decrease) from the first to the last iteration during 3D seismic inversion

Iterations	RMS (ms)	Reduction variance (%)
1.00	2.44	0.00
2.00	1.75	28.45
3.00	1.35	44.88
4.00	1.22	49.90
5.00	1.15	52.75

5.2 Experimental Data Inversion

After running the 3D active tomography using the ATOM3D code, a distribution of P-wave velocities was obtained above the mine gallery. Based on RMS stabilisation, the number of iterations was set to five, resulting in a velocity model presenting an average RMS of 1.15 ms and a variance reduction of 52.75%, demonstrating the efficiency of the travel-time inversion (Fig. 12 and Table 1).

Several parameters affecting the reliability and accuracy of the results were tested: the initial 1D velocity model, smoothing, and amplitude damping parameters. Multiple 1D reference models were assessed during the experimental data inversion according to two criteria: (1) the model should display realistic velocity variations between depth layers, and (2) the resulting 3D velocity distribution should correspond to the geological structures present in the region. Based on these tests, the starting velocity model that provided a robust correlation with the geological structures and a low RMS misfit was selected and is presented in Table 2. This model consists of two layers with fixed velocities, where the velocity values between depths were estimated by linear interpolation. The smoothing and amplitude damping parameters, which influence inversion stability, were tested on the synthetic inversions to determine their optimum values for accurate and reliable tomographic results, as discussed in the previous section.

Figure 13 displays six depth slices showing the velocity anomalies spread together with the gallery and the main and secondary fault locations (2 m, 5 m, 10 m, 15 m, 18 m, and 20 m). The anomalies are visualised at 2 m away from the cross-sections. The area is divided by the CF into two distinct anomaly polarities, clearly visible between 10 and 15 m depth. Negative anomalies are mainly associated with the gallery chamber, corresponding to the PQG at higher depths (anomaly N3), whereas at shallower levels, they relate not only to the PQG (anomaly N2) but also to the highly fractured zone of the VSC (anomaly N1). On vertical profiles, N1 and N2 extend vertically to depths of approximately 10–12 m for almost all the sections except I–J, beneath which N2 extends down to 25 m (Fig. 14). Conversely, N3 appears at greater depths, from approximately 15 m down to 25 m, with a higher amplitude between 17 and 18 m, coinciding with the gallery chamber.

As described earlier, during the excavation period, different materials were used to support the gallery. Reinforced concrete was applied in areas where the geological structure was weaker and more prone to collapse, whereas wooden stowage was used in zones composed of more competent rock formations. This provided additional information on the degree of rock consolidation, which aided the interpretation of the model.

At shallow depths, the CF is located within negative anomalies, near to the boundary between negative PQG anomaly (N2) and positive VSC anomaly (P1). As this brittle

Table 2 1D velocity model used to generate the ray paths and three-dimensional distribution of velocity perturbations presented in Figs. 5, 12 and 13. The velocity between layers is deduced by interpolation

Depth (m)	Velocity (km/s)
– 2.0	0.9
20	1.6

structure is approximately 5 m wide, it correlates significantly with the westward extension of N2 from the fault location. On its eastern side, the same anomaly (N2) corresponds to the PQG, showing a decrease in wave velocity.

In the southern part of the area, an intense negative anomaly (N1) is associated with mine rejects and a weakening of the geological structure, probably caused by the fault system located in a zone of decreasing topography, which is typically more prone to fracturing and fault creation, as shown in Fig. 15. This zone also coincides with the part of the gallery supported by reinforced concrete, confirming the low level of consolidation of the geological formation.

Conversely, positive anomalies (P1 and P2) appear at shallow depths (between 2 and 10 m), marking the transition from concrete to wooden stowage support at the location of the tectonic fault CF, producing a distinct velocity response. These anomalies completely disappear at greater depths (15 m, 18 m, and 20 m depth in Fig. 14), giving rise to P3, which exhibits a higher amplitude positive anomaly.

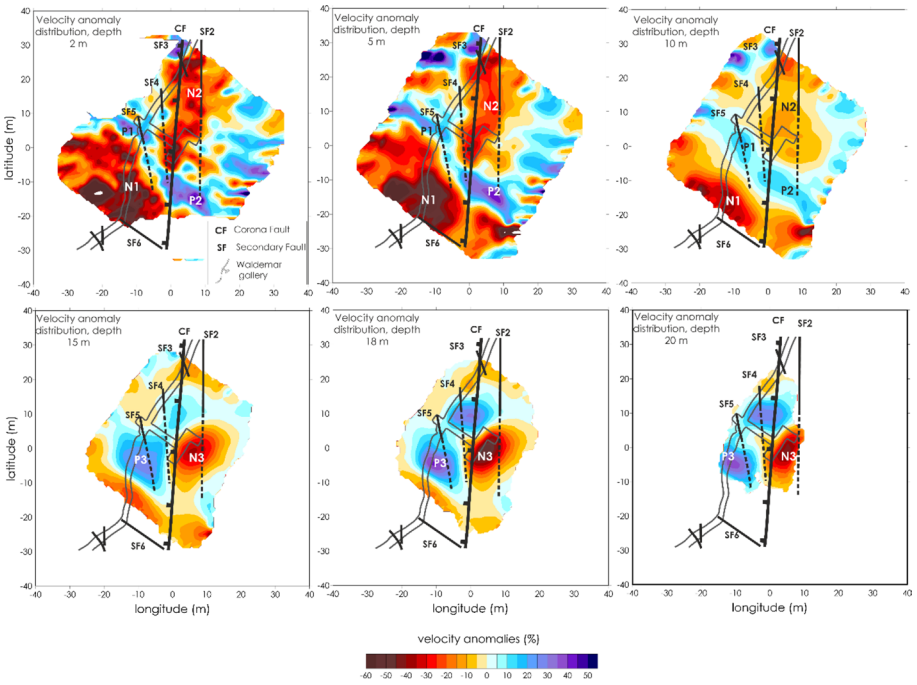

Fig. 13 Depth slices showing the velocity anomaly distribution at 2 m, 5 m, 10 m, 15 m, 18 m, and 20 m (depth of the gallery), generated after the experimental inversion. The P and N labels refer, respectively, to the positive and negative anomalies

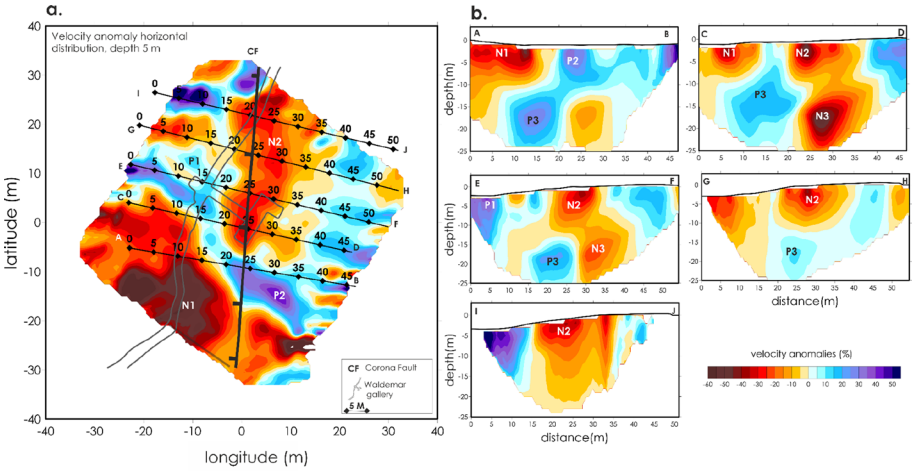

Fig. 14 **a** Horizontal velocity anomaly distribution at a depth slice of 5 m; **b** vertical distribution of velocity anomalies underneath cross-sections (A-B, C-D, E-F, G-H, and I-J). The P and N labels refer, respectively, to the positive and negative anomalies

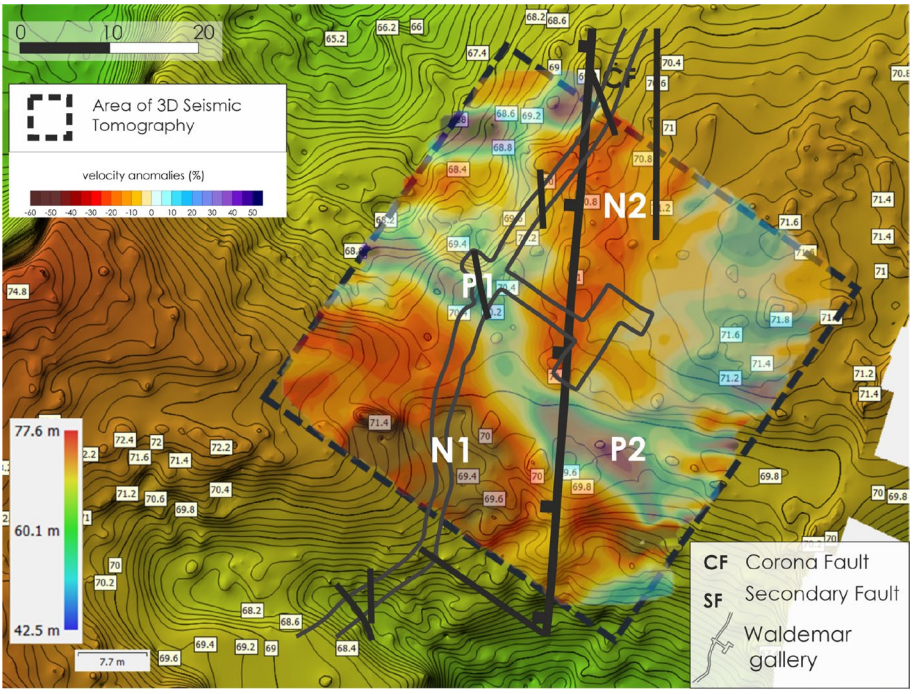

Fig. 15 Superposition of the anomaly depth slice (at 5 m depth) with the topographic map to highlight the explanation discussed in the text. P and N refer to positive and negative anomalies, respectively. The structural feature CF refers to the Corona fault

The structure indicates an anticline coinciding with the shaft location, correlating with positive anomalies and increasing absolute velocities ranging from 1.7 km/s and 2.0 km/s at the gallery floor level (approximately 18 m depth). Low velocities (around 0.6 km/s) are observed at the location of the gallery chamber, where reinforced concrete was used to support weaker geological structures (Fig. 16).

The correlation between the velocity anomalies and the type of support confirms that the anomaly distribution is consistent with the degree of consolidation of the rocks intersected by the gallery.

Stress redistribution within complex structural configurations is more likely to cause stress concentrations (Friedel et al. 1995; Wang et al. 2018). The fault system present in the region can generate localised stress accumulation, consistent with the observed high velocities embedded within negative anomalies. This is likely related to the weakening of rocks surrounding the CF, along which a dextral strike-slip movement occurred with a small normal component, as indicated by lateral variations in absolute velocities (Fig. 16).

5.3 Geological Faults' Interpretation

As a baseline for interpreting the fault system, knowledge from previous geological studies conducted in Lousal by other authors was considered (Matos and Relvas 2006; Matos 2021). Because of its regional-scale formation, the CF is the only structure for which the depth extension has been characterised. As mentioned previously, this fault appears in the 3D tomograms, both in the depth slices and vertical cross-sections, marking the boundary between positive and negative anomalies (Figs. 13 and 14).

Regarding the secondary faults, six of them cross the investigated area and are identified as SFs on the velocity maps. These faults are not visible at the surface, probably due to soil development, but since the studied area is relatively small, it was assumed that they retain a linear extension in both horizontal and vertical directions, following the orientation observed at the gallery level. Furthermore, as the CF has been characterised as subvertical,

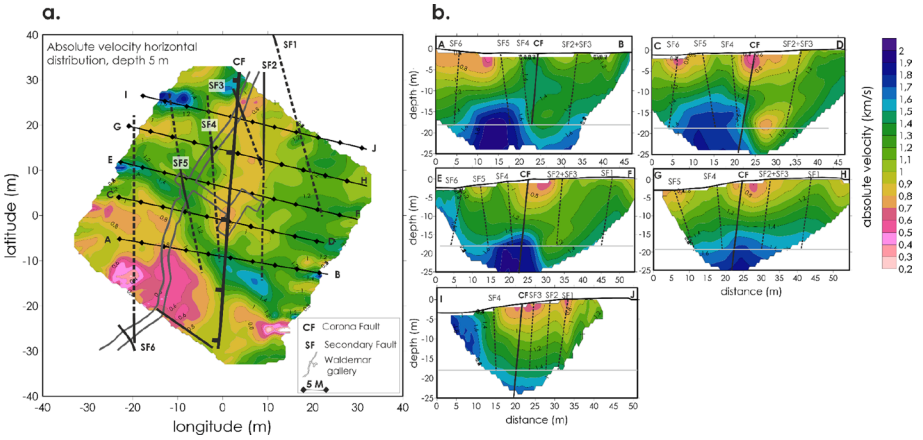

Fig. 16 **a** Horizontal absolute velocity distribution with the faults locations and their possible horizontal extension, highlighted by *black dashed lines*; **b** vertical velocities spread under the 5 cross-sections (A-B, C-D, E-F, G-H, and I-J). The interpretation of the fault extension within depth is shown. The secondary faults (SF) appear at the depth of the Waldemar gallery (18 m) highlighted by a *grey line*. The interpretation of their prolongation *(black dashed lines)* was done starting from the depth of the gallery up to the surface

the same kinematic characteristics were assumed for the SFs. The superposition of the anomaly depth slice with the topographic map, as illustrated in Fig. 15, shows a strong correlation. Based on these assumptions and observations, an attempt was made to correlate the subsurface velocity model with these brittle structures, and a proposed model of the local fault system and its depth extension is presented in Fig. 16.

The boundary between two different lithologies or rocks with distinct petrophysical properties is generally highlighted by velocity variations in both horizontal and vertical directions (Wang et al. 2008). This approach was employed to propose an interpretation of the vertical continuation of the fault planes. In the surveyed area, five sections (A-B, C-D, E-F, G-H, I-J) crossing the fault set were selected to visualise their vertical continuation, and the lateral velocity variation was chosen as the marker for fault position (Fig. 16b). The lateral velocity heterogeneity at the location of the CF likely indicates a normal fault, where the right-hand block has moved downwards relative to the left. The SFs appear to have the same direction and extent in all sections, and the CF interpretation is consistent with fault displacement, characterised as a subvertical fault with a normal component and an inclination of N5ºE (Matos 2021, 2022).

Only two cross-sections intersect the Waldemar gallery: sections C-D and E-F. As described earlier, at the location of the gallery, structural weakness was detected before excavation began, requiring the use of reinforced concrete for support. This is confirmed by the observation of a sharp local velocity drop at the gallery level, appearing approximately 30 m from the start of the section. Some of the SFs can clearly be observed in several sections (e.g. SF4 and SF6 in sections A-B, C-D, and E-F; SF1 and SF5 in sections E-F, G-H, I-J) but tend to be more difficult, or even impossible, to detect in others. Nevertheless, assuming that, at the surveyed scale, the faults remain linear and cross all five sections, a correlation with the velocity variation was carried out wherever possible around their assumed positions. The same correlation was applied to the horizontal cross-sections at different depths, where similar patterns can be identified or assumed along the SFs extensions. This revealed a clear velocity contrast at the CF location, extending to a depth of 25 m, and demonstrated that the SFs vertical extensions are consistent with the regional kinematics.

6 Conclusion

Incorporated within the LouMu project, this work presents for the first time the results of a three-dimensional seismic refraction tomography survey conducted in the Iberian Pyrite Belt's Lousal Mine, following an innovative experiment undertaken at this site. Prior to this seismic survey, a conventional geophone-shot configuration was initially employed, and a 2D profile was acquired. The objective was to detect the Corona Fault (CF) and to analyse its extension from the surface down to the depth of the Waldemar gallery, located approximately 18 m below the surface, by generating a 2D subsurface model.

The 2D seismic refraction tomography profiles were unable to resolve the crustal structure of the entire subsurface due to the absence of ray paths below a depth of around 15 m. This limitation was likely caused by the velocity variations at greater depths, which hindered wave refraction. Nevertheless, to enhance ray coverage and ensure the propagation of rays down to the gallery level, an innovative arrangement of geophones and shots enabled complete three-dimensional coverage of the target subsurface, extending to depths greater than 20 m. The resolution

tests demonstrated a robust reconstruction of anomalies larger than or equal to 3 m, confirming the high-resolution capability achieved through a fine geophone-shot configuration. The resulting anomaly distribution after inversion showed consistency with the rock consolidation levels. During excavation, several reports were documented the presence of more brittle rocks in the south-eastern and western parts of the surveyed area, with a greater consolidation in the central zone, necessitating the use of different building materials to support the gallery.

Accordingly, the Phyllite-Quartzite Group (PQG) corresponds to negative anomalies, whereas positive anomalies are correlated with the Volcano-Sedimentary Complex (VSC). The positive anomalies also indicated higher stress levels compared with the surrounding zones, which are characterised by lower velocities and are likely transmitting the load to adjacent structures.

Moreover, the Corona Fault (CF) traverses the boundary between positive and negative anomalies representing distinct lithologies. This fault extends with depth, displaying a slight inclination, consistent with a normal fault mechanism, in agreement with the previously described N5ºE inclination reported in earlier studies. Additional secondary faults were also identified, appearing predominantly as normal faults, and their vertical extension was inferred from lateral velocity variation. Finally, the study enabled the assessment of the probable subsurface extension of the fault system, confirming the presence of the Corona Fault (CF) and SFs crossing the surveyed area. By correlation, the analysis also facilitated the identification of high- and low-stress zones based on the visualisation of the anomaly distribution.

Funding Ines Hamak and Pedro Teixeira are supported by the PhD grant under the references UI/BD/154621/2022 (https://doi.org/10.54499/UI/BD/154621/2022) and PD/BD/150490/2019, respectively. This work is funded by national funds through FCT—Fundação para a Ciência e Tecnologia, I.P., in the framework of the UIDB/06107—Centro de Investigação em Ciência e Tecnologia para o Sistema Terra e Energia (CREATE) of the University of Évora. The authors are also thankful for the help of Josué Figueira and the Ciência Viva Lousal Centre team, both of whom helped facilitate the seismic campaign.

References

Cai Wu, Dou L, Cao A, Gong S, Li Z (2014) Application of seismic velocity tomography in underground coal mines: a case study of Yima Mining Area, Henan, China. J Appl Geophys 109:140–149. https://doi.org/10.1016/j.jappgeo.2014.07.021

Duarte M, Andringa S, Sarmento R, Blanco A, Afonso L, Alexandre I, Assis P, Bezzeghoud M, Borges J, Caldeira B (2024) Muon tomography of the physics department of the University of Coimbra. J Adv Instrum Sci. https://doi.org/10.31526/jais.2024.483

Fernandes ASC (2011) Caracterização Petrográfica, Mineralógica e Geoquímica Do Padrão de Alteração Hidrotermal a Muro Das Massas Dos Sulfuretos Maciços Do Lousal, Faixa Piritosa Ibérica

Friedel MJ, Jackson MJ, Scott DF, Williams TJ, Olson MS (1995) 3-D tomographic imaging of anomalous conditions in a deep silver mine. J Appl Geophys 34(1):1–21. https://doi.org/10.1016/0926-9851(95)00007-O

García-Yeguas A, Koulakov I, Ibáñez JM, Rietbrock A (2012) High resolution 3D P wave velocity structure beneath Tenerife Island (Canary Islands, Spain) based on tomographic inversion of active-source data. J Geophys Res 117:B09309. https://doi.org/10.1029/2011JB008970

Intelligent Resources INC (2020) Rayfract Software 2020 Seismic refraction and borehole tomography-subsurface seismic velocity models for geotechnical engineering and exploration

Koulakov I (2009a) LOTOS code for local earthquake tomographic inversion benchmarks for testing tomographic algorithms. Bull Seismol Soc Am 99(1):194–214. https://doi.org/10.1785/0120080013

Koulakov IY (2020) Basic tomo: an educational tool for investigating the role of controlling parameters and observation geometry in tomography problems. Russ J Geophys Technol 1:40–54. https://doi.org/10.18303/2619-1563-2020-1-40

Koulakov I, Stupina T, Kopp H (2010) Creating realistic models based on combined forward modeling and tomographic inversion of seismic profiling data. Geophysics 75(3):B115. https://doi.org/10.1190/1.3427637

Koulakov I (2009b) Code ATOM-3D for 3D tomographic inversion based on active refraction seismic data

Koulakov I (2009c) Code PROFIT for forward modeling and tomographic inversion based on active refraction seismic profiling data. Novosibirsk, Russia

Matos JX, Oliveira V (2003) Mina do Lousal (Faixa Piritosa Ibérica)-Percurso geológico e mineiro pelas cortas e galerias da antiga mina. IGME Pub Museo Geominero 2:117–128

Matos JX, Carvalho J, Represas P, Batista MJ, Sousa P, Ramalho EC, Marques F, Morais I, Albardeiro L, Gonçalves P, Dias P (2020) Geophysical surveys in the Portuguese sector of the Iberian Pyrite Belt: a global overview focused on the massive sulphide exploration and geologic interpretation. Com Geológicas LNEG 107:41–78. https://doi.org/10.34637/em01-yd39

Matos JX, Relvas JMRS (2006) Mina Do Lousal (Faixa Piritosa Ibérica). Livro Guia Excursão C. 4.1. In: VII Congresso Nacional de Geologia, Estremoz, Univ. Évora, Portugal, pp 23–25

Matos JX (2021) Alteração Hidrotermal Ácido-Sulfato Associada Aos Jazigos de Sulfuretos Maciços de Lagoa Salgada, Caveira, Lousal, Aljustrel e São Domingos (Faixa Piritosa Ibérica). PhD Thesis, Science Faculty Lisbon University, 435p

Matos JX (2022) Lousal mine southern sector geological map, 1/5.000 scale. LNEG, LouMu Project

Nolet G (1987) Seismic wave propagation and seismic tomography. Seismic tomography: with applications in global seismology and exploration geophysics. Springer, pp 1–23. https://doi.org/10.1007/978-94-009-3899-1_1

Oliveira M, Ferreira T, Relvas JMRS, Pinto AMM, Matos JX, Pereira Z, Fernandes C (2013) Lousal, Portugal: Património Geológico e Mineiro de uma antiga mina na Faixa Piritosa Ibérica. XIV Cong. Patrimonio Geológico y Minero. Castrillón (Asturias), XVIII Sesión Científica de SEDPGYM, p20

Paige CC, Saunders MA (1982) LSQR: an algorithm for sparse linear equations and sparse least squares. ACM Trans Math Softw (TOMS) 8(1):43–71. https://doi.org/10.1145/355984.355989

Relvas JMRS, Pinto AMM, Matos JX (2012) Lousal, Portugal: a successful example of rehabilitation of a closed mine in the Iberian Pyrite Belt. Soc Geol Appl Miner Depos SGA News 31:1–16

Rucker ML (2000) Applying the seismic refraction technique to exploration for transportation facilities. Geophysics 1:1–3

Teixeira P, Afonso L, Andringa S, Assis P, Bezzeghoud M, Blanco A, Borges JF, Caldeira B, Cazon L, Dobrilla P, Lopes L (2022) Muography for underground geological surveys: ongoing application at the lousal mine (Iberian Pyrite Belt, Portugal).https://doi.org/10.31526/jais.2022.287

Teixeira P, Blanco A, Caldeira B, Tomé B, Alexandre I, Matos J, Silva J, Borges J, Cazon L, Afonso L, Lopes L, Magda Duarte, Mário Pimenta, Mourad Bezzeghoud, Paolo Dobrilla, Pedro Assis, Raul Sarmento, Rui Oliveira and Sofia Andringa (2024) Muography applied in underground geological surveys: ongoing work at the Lousal Mine (Iberian Pyrite Belt, Portugal) BT-Recent research on geotechnical engineering, remote sensing, geophysics and earthquake seismology. In: M Bezzeghoud, ZA Ergüler, J Rodrigo-Comino, MK Jat, R Kalatehjari, DS Bisht, A Biswas, HI Chaminé, AA Shah, AE Radwan, J Knight, D Panagoulia, A Kallel, V Turan, H Chenchouni, A Ciner, and M Gentilucci (Eds), Springer, Cham, pp 173–77, https://doi.org/10.1007/978-3-031-48715-6_38

Um J, Thurber C (1987) A fast algorithm for two-point seismic ray tracing. Bull Seismol Soc Am 77(3):972–986. https://doi.org/10.1785/BSSA0770030972

Wang F, Duan Y, Yang Z, Zhang C, Zhao J, Zhang J, Zhang X, Liu Q, Zhu A, Xu X (2008) Velocity structure and active fault of Yanyuan-Mabian Seismic Zone—the result of high-resolution seismic refraction experiment. Sci China Ser D Earth Sci 51:1284–1296. https://doi.org/10.1007/s11430-008-0098-0

Wang Z, Li X, Zhao D, Shang X, Dong L (2018) Time-lapse seismic tomography of an underground mining zone. Int J Rock Mech Min Sci 107:136–149. https://doi.org/10.1016/j.ijrmms.2018.04.038

Authors and Affiliations

Ines Hamak[1] · Pedro Teixeira[1] · José Borges[1] · Ivan Koulakov[2,3] · Rui Oliveira[6] · Bento Caldeira[1] · Mourad Bezzeghoud[1] · João X. Matos[4] · Sofia Andringa[5]

✉ Ines Hamak
ihamak@uevora.pt

Pedro Teixeira
pmmt@uevora.pt

José Borges
jborges@uevora.pt

Ivan Koulakov
ivan.science@gmail.com

Rui Oliveira
ruio@uevora.pt

Bento Caldeira
bafcc@uevora.pt

Mourad Bezzeghoud
mourad@uevora.pt

João X. Matos
joao.matos@lneg.pt

Sofia Andringa
sofia@lip.pt

[1] Physics Department (ECT), CREATE (Centre for Sci-Tech Research in EArth sysTem and Energy), Earth Remote Sensing Laboratory (EaRSLab), University of Évora, Rua Romão Ramalho nº59, 7000-671 Évora, Portugal

[2] Skolkovo Institute of Science and Technology (Skoltech), Bolshoy Blrd 30/1, Moscow, Russia 121205

[3] Trofimuk Institute of Petroleum Geology and Geophysics SB RAS, Novosibirsk, Russia

[4] Nacional Laboratory of Energy and Geology (LNEG), Campus de Aljustrel, Bairro da Vale d'Oca, Apartado 14, 7601-909 Aljustrel, Portugal

[5] Laboratory of Instrumentation and Experimental Particle Physics (LIP), Av. Prof. Gama Pinto 2, 1649-003 Lisbon, Portugal

[6] Faculty of Sciences and Technology - Department of Earth Sciences - Geosciences Center (CGeo), University of Coimbra, Rua Sílvio Lima, 3030-790, Coimbra, Portugal